Radiation Transport in MEDUSA

S J Rose and R G Evans

Radiation transport in MEDUSA

S J Rose and R G Evans

Science and Engineering Research Council

Rutherford Appleton Laboratory

Chilton, Didcot, Oxon, England

Abstract

The transport of energy by X-ray photons has been included in the 1D
Lagrangian hydrodynamics code, MEDUSA. Calculations of the implosion by
0.53 μm laser irradiation of plastic and glass microballoons of current
interest at the Central Laser Facility show that radiation preheats the
fill gas and alters the temperature and density profiles during the
implosion. A lower maximum gas temperature is obtained and this results,
for a DT gas fill, in a greatly reduced neutron yield.

1. Introduction

There are two areas for which radiation transport needs to be considered
in laser-produced plasmas. The first is the calculation for comparison
with spectroscopic observations, of the X-ray spectrum, including details
of line shape and line intensity ratios. The second area is the calculation
of energy flow by X-ray photons and it is this subject, and in particular
X-ray pre-heating of laser-driven targets, which is addressed in this paper.
The radiative energy transfer model that has been included in the 1D
Lagrangian hydrodynamics code MEDUSA is described in section 2. Comparison
between calculated and measured X-ray emission is shown in section 3 whilst
the absorption opacity is discussed in section 4. The effects of X-ray pre-
heat on microballoon implosions as predicted by MEDUSA are shown in section 5.

2. The radiation transport model

Because the photon mean free path depends strongly on the photon energy (in general the higher the photon energy, the longer the mean free path) the radiation transport calculation which has been included in MEDUSA, is split into 30 photon energy groups. Inelastic scattering of photons is expected to be negligible for laser targets and is ignored. Only photon absorption and emission are considered and each group is transported separately.

In a laser-heated plasma the region of maximum X-ray emission occurs at densities slightly greater than critical and the energy is radiated inwards to the cooler absorbing region. The diffusion approximation to the radiation transport equation is therefore questionable because of its assumption of isotropy of the radiation field. The model adopted differentiates between photons travelling inwards into the target and those travelling outwards and in each case it is assumed that radiation is isotropic in the half-plane. In the rest of this section we shall consider a general Lagrangian cell ℓ in spherical geometry with inner cell boundary j of area A_j and outer cell boundary $j+1$ of area A_{j+1}. The radiation energy travelling inwards across cell boundary j per unit time in group g is denoted F_j^{+g} and that travelling outwards by F_j^{-g}.

Absorption of X-ray photons is most important in the cold dense material ahead of the critical density which is probably in Local Thermodynamic Equilibrium (LTE) and the LTE absorption opacity is used throughout the present work to calculate attenuation. Because the radiation spectrum within a group is not known a constant weighting function is taken for the calculation of the group-averaged mean opacity (denoted κ_ℓ^{LTEg} for group g and cell ℓ) from monochromatic values calculated by an average-atom screened-hydrogenic model (Pritzker et al 1975).

The X-ray energy passing inwards through cell boundary j in group g per unit time which was emitted by material within cell ℓ is denoted S_ℓ^{+g} whilst that emitted outwards through $j+1$ is denoted S_ℓ^{-g}. These quantities are given by:

$$S_\ell^{+g} = A_j \alpha_\ell^g \; \sigma T_\ell^4 \; (1 - \exp(-\rho_\ell \kappa_\ell^g \Delta r_\ell)) \qquad (1)$$

$$S_\ell^{-g} = A_{j+1} \alpha_\ell^g \; \sigma T_\ell^4 \; (1 - \exp(-\rho_\ell \kappa_\ell^g \Delta r_\ell)) \qquad (2)$$

where σ is Stefan's constant and α_ℓ^g is the fraction of the integrated Planck function at the electron temperature of the cell T_ℓ which lies in group g:

$$\alpha_\ell^g = \int_g B(\nu, T_\ell) \, d\nu \bigg/ \int_o^\infty B(\nu, T_\ell) \, d\nu. \qquad (3)$$

The density of material in cell ℓ is denoted ρ_ℓ and Δr_ℓ is the average distance that a photon which is not absorbed in the cell travels between entering and leaving. This "mean chord" is given by a general formula due to Dirac as (4 x volume)/(total area), which for Lagrangian cell ℓ is

$$\Delta r_\ell = 4(r_{j+1}^3 - r_j^3)/3(r_{j+1}^2 + r_j^2). \qquad (4)$$

The region of maximum X-ray emission in a laser-heated plasma lies at a slightly greater density than critical. The ionic level populations are not in LTE and cannot necessarily be assumed to be in a steady-state. Following the time dependence of the level populations in this region is a very complicated problem and so for this work a steady-stare model is used which is modified with reference to experiment. Although the rate of conversion of energy from material to radiation is not known for a plasma whose electronic populations are in general collisional-radiative steady-state, calculations for the low density coronal limit have been performed; the most accurate of which are those of Summers and McWhirter (1979). At high density LTE holds. Interpolation between these two limits is achieved by taking

$$\kappa_\ell^g = \min \left\{ \kappa_\ell^{LTEg}, \; \gamma \kappa_\ell^{cg} \right\}. \qquad (5)$$

For LTE in the optically thin limit S_ℓ^{+g} and S_ℓ^{-g} reduce to the LTE rate of conversion of energy in cell ℓ from material to radiation in group g weighted by the ratio of the area of the cell boundary to the total area bounding the cell*. The factor γ is fitted to experimental data (section 3) and accounts

*This would be exact were the Planck mean opacities used. However the effect of using a constant rather than a Planck weighting is not considered to be important.

for the departure of the electronic populations from a steady-state. The 'coronal opacity' κ_ℓ^{cg} is defined so as to obtain the correct coronal emission from the cell in the optically thin limit. If W_ℓ^g is the energy converted from material to radiation per unit volume per unit time for a plasma in a coronal steady-state then

$$S_\ell^{+g} = \frac{A_j}{A_j + A_{j+1}} \; W_\ell^g \, V_\ell \qquad\qquad (6)$$

and

$$S_\ell^{-g} = \frac{A_{j+1}}{A_j + A_{j+1}} \; W_\ell^g \, V_\ell \qquad\qquad (7)$$

where V_ℓ is the volume of cell ℓ. However from equations (1), (2) and (5) S_ℓ^{+g} and S_ℓ^{-g} are also given by

$$S_\ell^{+g} = A_j \, \alpha_\ell^g \, \sigma \, T_\ell^4 \, \rho_\ell \, \kappa_\ell^{cg} \, \frac{4V_\ell}{A_j + A_{j+1}} \qquad\qquad (8)$$

and

$$S_\ell^{-g} = A_{j+1} \alpha_\ell^g \, \sigma \, T_\ell^4 \rho_\ell \, \kappa_\ell^{cg} \, \frac{4V_\ell}{A_j + A_{j+1}} \; . \qquad\qquad (9)$$

Combining equations (6) and (8) or (7) and (9) gives

$$\kappa_\ell^{cg} = W_\ell^g \; / \; 4 \, \rho_\ell \, \alpha_\ell^g \, \sigma \, T_\ell^4 \; . \qquad\qquad (10)$$

Summers and McWhirter (1979) only quote values of emission over the entire energy spectrum: W_ℓ. The fraction of energy emitted in group g is denoted f_ℓ^g where

$$W_\ell^g = f_\ell^g \, W_\ell \qquad\qquad (11)$$

and f_ℓ^g is approximated by the equivalent LTE fraction which is approximately*

$$f_\ell^g = \kappa_\ell^{LTEg} \, \alpha_\ell^g \; / \; \sum_g (\kappa_\ell^{LTEg} \, \alpha_\ell^g) \; . \qquad\qquad (12)$$

The radiation transport model relates F_j^{+g} and F_{j+1}^{+g} by

$$F_j^{+g} = F_{j+1}^{+g} \exp\left(-\rho_\ell \kappa_\ell^{LTEg} \Delta r_\ell\right) \left(\frac{A_j}{A_{j+1}}\right) + S_\ell^{+g} . \tag{13}$$

The factor A_j / A_{j+1} accounts for photons travelling inwards through cell boundary j+1 and which are unabsorbed but which do not leave through j. The energy in group g per unit time which emerges in this way as outwardly directed energy flow through cell boundary j+1 is denoted G_{j+1}^g and is given from equation (13) by

$$G_{j+1}^g = F_{j+1}^{+g} \exp\left(-\rho_\ell \kappa_\ell^{LTEg} \Delta r_\ell\right) \left(1 - \frac{A_j}{A_{j+1}}\right) . \tag{14}$$

A similar expression to equation (13) relates radiant energy passing outwards through cell boundary j+1 to that through cell boundary j.

$$F_{j+1}^{-g} = F_j^{-g} \exp\left(-\rho_\ell \kappa_\ell^{LTEg} \Delta r_\ell\right) + S_\ell^{-g} + G_{j+1}^g . \tag{15}$$

The first term represents the energy from unabsorbed photons which entered through cell boundary j passing outwards through cell boundary j+1. The second term represents the energy passing outwards through cell boundary j+1 from photons produced within the cell. The last term represents the energy from photons passing inwards through cell boundary j+1 which pass outwards through the same cell boundary.

The total electronic energy rise in cell ℓ from absorption and emission of photons in timestep Δt is just the energy leaving the cell subtracted from the energy entering the cell:

$$\Delta E_\ell = \sum_g \left[\left(F_{j+1}^{+g} + F_j^{-g} \right) - \left(F_j^{+g} + F_{j+1}^{-g} \right) \right] \Delta t . \tag{16}$$

The radiation transfer calculation is performed at the end of each timestep after the hydrodynamics has been advanced. Starting with the boundary condition of zero energy flow into the target across the outside surface, equation (13) is used to calculate the energy flow across each cell boundary, working inwards. All the radiation flowing into the central cell which is subsequently unabsorbed

emerges as outwardly directed flow and starting with this, the outward flow across each cell boundary is then calculated (equation (15)). Finally the electronic energy is changed using equation (16).

3. Experimental measurements

While it is hoped that experiments to measure X-ray photons emitted by the rear surface of a laser-irradiated target will be conducted in the future, at present the only measurements available which allow comparison with theoretical radiation transport calculations involve measuring photons emitted from the front surface. Many such experiments have been performed and they fall into two categories. The first involves the use of filtered X-ray diodes. The use of filters gives only broad-band spectral information and their chief advantage is that they can be accurately calibrated. However very few diode measurements have been made on low-Z materials and none on plastic or glass at 0.53 μm which are of particular current interest at the CLF. The second category of measurements involves the use of film to record X-ray flux. Spectral information can be obtained by using a filter or by using a crystal. However absolutely calibrated X-ray measurements of this kind are rarely performed. Problems exist in taking measurements from flat foils because the X-ray emission is not generally uniform across the laser spot. For this reason absolutely calibrated X-ray measurements of spherical targets illuminated by 0.53 μm light from the VULCAN laser, have recently been performed where the problem of edge effects is somewhat reduced. Measurements from both plastic and glass microballoons have been obtained and in this section the results of these experiments are compared with the predictions of MEDUSA.

The first experiment (Lewis 1982) involved a 5.8 μm thick plastic (CH) microballoon of 123 μm diameter irradiated with 8.2 x 10^{13}Wcm^{-2} in a 1.2ns pulse. A pinhole camera with a Be filter was used to record the X-rays emitted from the target. Because of the limited spectral information obtained by this method, the spectral shape was assumed to be of bremsstrahlung form

$$I = Ce^{-h\nu/kT} \quad (keV \; keV^{-1} cm^{-2} s^{-1})$$

where the material temperature kT was taken to be 400eV. The intensity obtained by this method is shown in figure 1. A weighting function which is the product of the filter transmission $\exp(-x/\lambda(\nu))$ (where x is the Be filter thickness and $\lambda(\nu)$ is the photon mean free path in cold Be) and the spectral shape $\exp(-h\nu/kT)$ is also shown indicating that the experiment is predominantly sensitive to photons of about 1.4keV. The absorbed laser energy was not

measured but on the basis of previous experience was thought to be about 35%. This was difficult to arrange exactly in the MEDUSA simulation and the absorbed irradiance in the calculation is $3.2 \times 10^{13} Wcm^{-2}$ (which simulates 39% absorption). Taking $\gamma = 0.3$ (equation 5) the theoretical predictions lie below the experimental measurements. However in view of the large experimental uncertainties, particularly in relation to the absorbed irradiance and because of the simplicity of the model, the agreement is considered reasonable.

The second set of experiments (McGowen 1982) used a minispectrometer to produce spectrally resolved intensity measurements for photon energies between about 900eV and 1500eV from three glass and two plastic microballoon implosions. The irradiance conditions for these shots are given in table 1 and the experimental data is shown in figures 2-6 together with calculated spectra from the radiation transport model in MEDUSA. For both plastic and glass targets the steady-state emission is too great and reduction factors of $\gamma = 0.3$ for plastic and $\gamma = 0.01$ for glass are required to show reasonable agreement with experiment. This indicates that the ions do not spend a sufficient time in the heating region to reach a steady-state. Further investigation must await calculations which solve the electronic rate equations. As before, because of the simplicity of the model and uncertainties in the experiment, the agreement is considered reasonable and gives some confidence that the X-ray emission calculated by the model is approximately correct.

The calculated X-ray conversion efficiency for plastic and glass microballoons together with experimental values for Be, Ti and Au are given in table 2. As expected the conversion efficiencies for plastic lie above that of Be whilst the values for glass are generally higher.

4. Absorption opacity

Comparison of measured and calculated microballoon X-ray spectra given in section 3 give some confidence that the calculation of the source of X-ray preheat is approximately correct. No experimental measurements of the absorption opacity of hot material has been made and so the calculation of the absorption of X-rays in the target relies entirely on theoretical predictions of the opacity which come from the code of Pritzker et al (1975). These have been compared with Planck averaged group opacities calculated by Craxton (1983) from LANL monochromatic values and figure 7 shows that for the typical case of Carbon at 100eV and 10^{-1} gcm^{-3} the calculations are in good agreement for free-free and bound-free contributions. However bound-bound absorption below the K-edge which is present in the LANL calculation is missing from the opacities used in the present work. Because the transmission of X-ray photons is sensitive to 'windows' in the absorption opacity, the inclusion of bound-bound absorption may alter calculated radiative preheat and it is hoped to investigate this effect in future work.

5. The effect of radiation transport on microballoon implosions

In this section, the effect of radiation transport is assessed for three examples of 0.53μm ablative implosions of current interest at the CLF, details of which are given in table 3. The first example involves a thick-walled plastic microballoon of the kind whose implosion has recently been investigated by backlighting techniques. The second is a high intensity short pulse implosion of a low aspect-ratio plastic microballoon which is designed to compress the Freon (CCl_2F_2) gas fill to a high temperature and density for spectroscopic studies. The third example is a high intensity, short pulse glass microballoon implosion which is designed to produce measurable thermo-nuclear reactions from the DT gas fill. The second and third cases have initial gas densities which are amongst the highest currently employed in CLF targets.

Figures 8, 9 and 10 show that for each implosion, the trajectory of the inside surface of the shell and the maximum gas compression predicted by 1D simulations are not greatly affected by radiation transport.

The effect on the time evolution of the electron and ion temperatures in the gas is shown for implosions 2 and 3 in figures 11 and 12. Because of gradients, the temperature of the gas which started at half the initial radius is chosen as representative. Radiation preheats the gas before the first shock passes through. The preheat temperature is higher for the plastic than the glass implosion and the energy is deposited in the electronic distribution so that $T_e > T_i$. When the shock passes through the gas, energy is deposited in the ions and during this phase $T_i > T_e$. The maximum temperature achieved ($T_e \sim T_i$ at this point) is reduced from approximately 1keV to 500eV for each implosion. For the DT filled microballon the total neutron yield* is reduced from 3.7×10^7 to 3.7×10^5 with the inclusion of radiation transport.

*To avoid heating of the ions by convergence of the shock which is thought to be grossly overestimated at the centre in a 1D simulation, thermonuclear reactions are not included from DT which started at less than a half of the original gas radius.

The maximum compression and thereby the maximum temperature predicted by the 1D simulations is unlikely to be achieved in practice and will be limited by non-spherical effects such as non-uniform illumination and Rayleigh-Taylor instability. Although it is generally agreed that a volumetric compression of over 1000 (as predicted by the simulations) is not at present possible, the exact point at which 1D calculations become unreliable is not known.

The effect of radiative preheat on the electron temperature through the gas is shown for implosions 2 and 3 in figures 13 and 14. The time during the implosion to which the figures refer comes before maximum compression and the first shock has entered the gas but has not reached the centre. If radiation transport is included, the gas is heated more uniformally, the region ahead of the shock being preheated. The slight difference in the radius of the shell with and without radiation transport results in different gas density profiles in the outside part of the gas. However the central part of the gas does not show a large difference (figures 15 and 16).

The effect of radiation transport on the shell can be seen for the three implosions in figures 17-22. Radiative preheat increases the temperature of the inside of the shell which expands resulting in a lower maximum shell density. The density profile of the lower density material on the outside of the shell is also altered resulting in a longer density scale length. Because of this, the interpretation of backlighting experiments may be altered by inclusion of radiation transport in the simulations and it is hoped to investigate this in a more quantitative manner in future work.

6. Conclusion

In the present work the transport of energy by X-ray photons has been included in the 1D lagrangian hydrodynamics code MEDUSA. The agreement between calculations and experimental measurements of X-ray spectra from laser-irradiated plastic and glass microballoons gives some confidence that the emission of X-rays is being treated in a manner which is roughly correct, although a departure of the electronic populations from LTE in the X-ray emission region is indicated. The electronic populations in this region do not appear to reach a steady-state and emission is reduced from the coronal value to obtain agreement with experiment. It is hoped that in future work this procedure will be replaced by a calculation which follows the evolution of the electronic populations in time by solution of the rate equations.

The effect of radiation transport has been assessed for three microballoon implosions of current interest at the CLF. Radiation is found to preheat the fill gas and the inside of the shell, reducing the maximum shell density and altering the density profile on the outside of the shell. The maximum gas temperature is reduced and this has a large effect on, for example, the neutron yield of a DT-filled target.

The calculations presented in this report indicate that radiation transfer may play an important role in the behaviour of current 0.53 μm laser-irradiated implosions. It is hoped that in the future improved calculations together with further experiments which measure target performance as well as emitted X-ray spectra will increase our present understanding of the transfer of energy by X-ray photons and that this will allow design of targets in which the deleterious effects of radiative preheat are reduced.

Acknowledgements

I am most grateful to Dr C Lewis and Dr B McGowan for their experimental results and to Dr S Craxton for his opacity calculations.

Table 1 Shot details

Shot*	Target material	Diameter (μm)	Thickness (μm)	$I_{incident}$ (Wcm^{-2})	$I_{absorbed}$** (Wcm^{-2})
12 181182	Plastic	176	6.1	4.4×10^{13}	1.5×10^{13}
16 181182	Plastic	136	4.7	9.5×10^{13}	3.3×10^{13}
09 191182	Glass	175	3.3	7.8×10^{13}	2.8×10^{13}
08 231182	Glass	106	3.3	8.8×10^{13}	3.2×10^{13}
24 231182	Glass	110	2.6	9.3×10^{13}	3.3×10^{13}

* All shots had a pulse length of 900ps FWHM.

** The absorbed irradiance in the MEDUSA calculation, which is arranged to be approximately 35% of the experimentally determined incident irradiance.

Table 2 Measured and calculated X-ray conversion efficiency values
(X-ray energy/absorbed energy) for 0.53μm incident laser radiation

Material	Incident intensity (Wcm^{-2})	Pulse length (ps)	X-ray conversion efficiency (X-ray energy/absorbed energy)
Beryllium	3×10^{14}	600	$1.5 \pm 0.2\%$ (m)
Plastic	4.4×10^{13}†	900	$4.3\%^{+}$
	8.2×10^{13}†	1200	$3.2\%^{+}$
	9.5×10^{13}†	900	$3.3\%^{+}$
Glass	7.8×10^{13}†	900	$5.1\%^{++}$
	8.8×10^{13}†	900	$4.1\%^{++}$
	9.3×10^{13}†	900	$3.8\%^{++}$
Titanium	3×10^{14}	600	$27 \pm 8\%$ (m)
	2×10^{15}	600	$17 \pm 7\%$ (m)
Gold	3×10^{13}	600	$40 \pm 10\%$ (m*)
	3×10^{14}	600	$48 \pm 12\%$ (m*)
	2×10^{15}	600	$38 \pm 10\%$ (m*)
	5×10^{15}	600	$28 \pm 10\%$ (m*)

m   Measured values, LLNL annual report 1980, section 7.

*   Values read from figure 7-50, LLNL annual report 1980.

+ $\gamma = 0.3$

++ $\gamma = 0.01$

†   All calculations arranged to have $I_{abs} \sim 0.35 I_{inc}$ (table 1).

Table 3 Implosion calculations used as examples in the assessment of the effect of radiation transport

Implosion	Shell material	Shell diameter (μm)	Shell thickness (μm)	Initial gas fill	$I_{absorbed}$** (Wcm^{-2})	Pulse length (ps)
1	CH	123	5.8	1 bar Nitrogen	3.1×10^{13}	1200
2	CH	146	10.0	2 bar Freon*	2.8×10^{14}	500
3	SiO_2	122	5.0	10 bar DT+ 10 bar Neon	5.2×10^{14}	410

* Neon, having similar average atomic number and atomic weight, is substituted at the same density for Freon (CCl_2F_2) in the MEDUSA simulation.

** The absorbed intensity quoted is that for the simulation including radiation transport; the value for the simulation without radiation transport is in each case within a few % of this figure.

Figure captions

Figure 1 Comparison of calculated and measured X-ray spectra from a plastic microballoon 123 μm diameter, 5.8 μm thick imploded by 0.53 μm laser light of $I_{incident} = 8.2 \times 10^{13} Wcm^{-2}$. Also shown is the weighting function $\exp(-x/\lambda(\nu))\exp(-h\nu/kT)$.

Figure 2 Comparison of calculated and measured X-ray spectra from shot 12 181182 (table 1).

Figure 3 Comparison of calculated and measured X-ray spectra from shot 16 181182 (table 1).

Figure 4 Comparison of calculated and measured X-ray spectra from shot 09 191182 (table 1).

Figure 5 Comparison of calculated and measured X-ray spectra from shot 08 231182 (table 1).

Figure 6 Comparison of calculated and measured X-ray spectra from shot 24 231182 (table 1).

Figure 7 Opacity of carbon at 100eV and $0.1gcm^{-3}$.

Figure 8 The trajectory of the plastic-gas interface in implosion 1 (table 3) as calculated by MEDUSA with and without the inclusion of radiation transport.

Figure 9 The trajectory of the plastic-gas interface in implosion 2 (table 3) as calculated by MEDUSA with and without the inclusion of radiation transport.

Figure 10 The trajectory of the glass-gas interface in implosion 3 (table 3) as calculated by MEDUSA with and without the inclusion of radiation transport.

Figure 20 Density of the plastic shell in implosion 2 (table 3) at 750ps as calculated by MEDUSA with and without the inclusion of radiation transport.

Figure 21 Electron temperature of the glass shell in implosion 3 (table 3) at 650ps as calculated by MEDUSA with and without the inclusion of radiation transport.

Figure 22 Density of the glass shell in implosion 3 (table 3) at 650ps as calculated by MEDUSA with and without the inclusion of radiation transport.
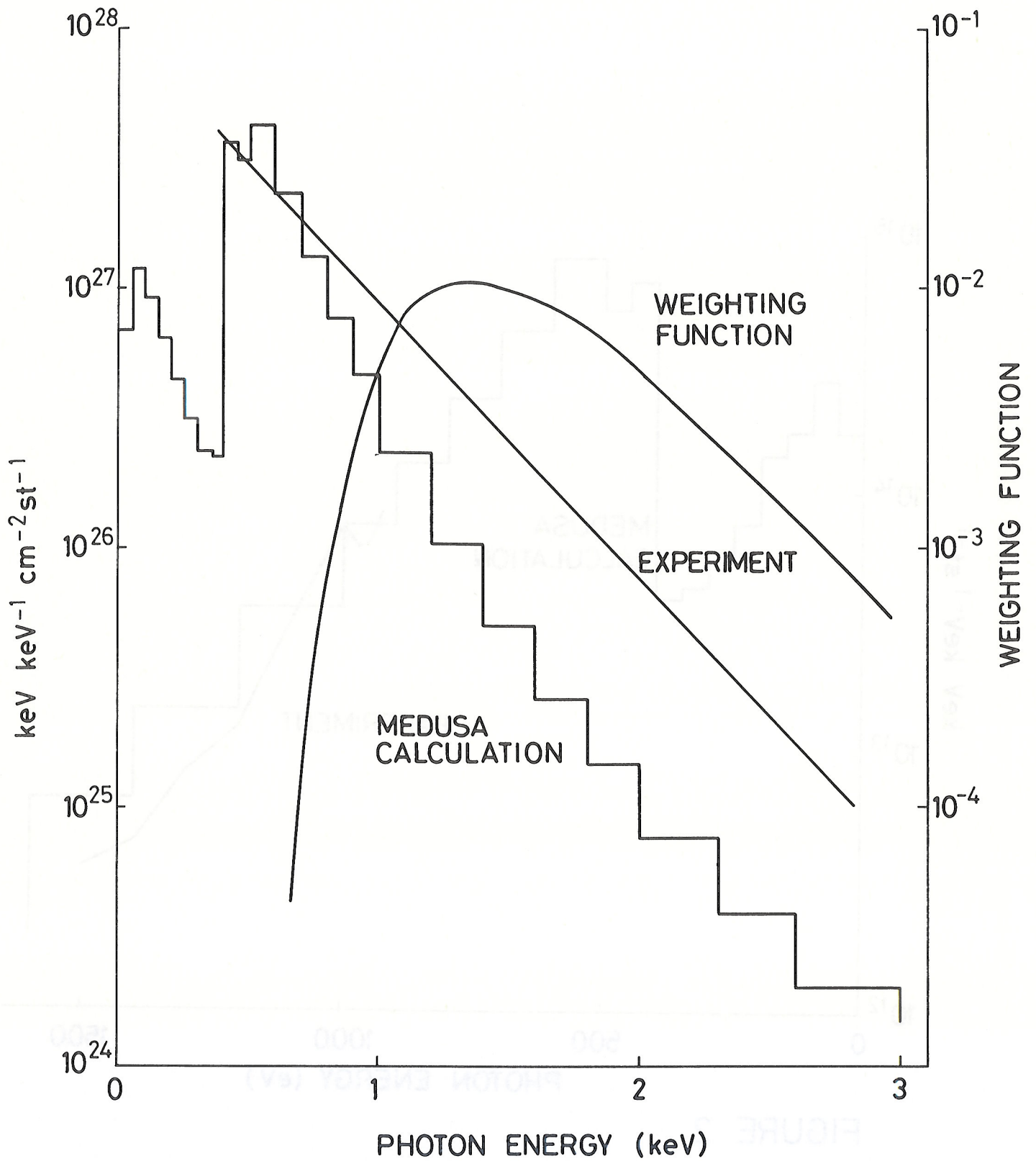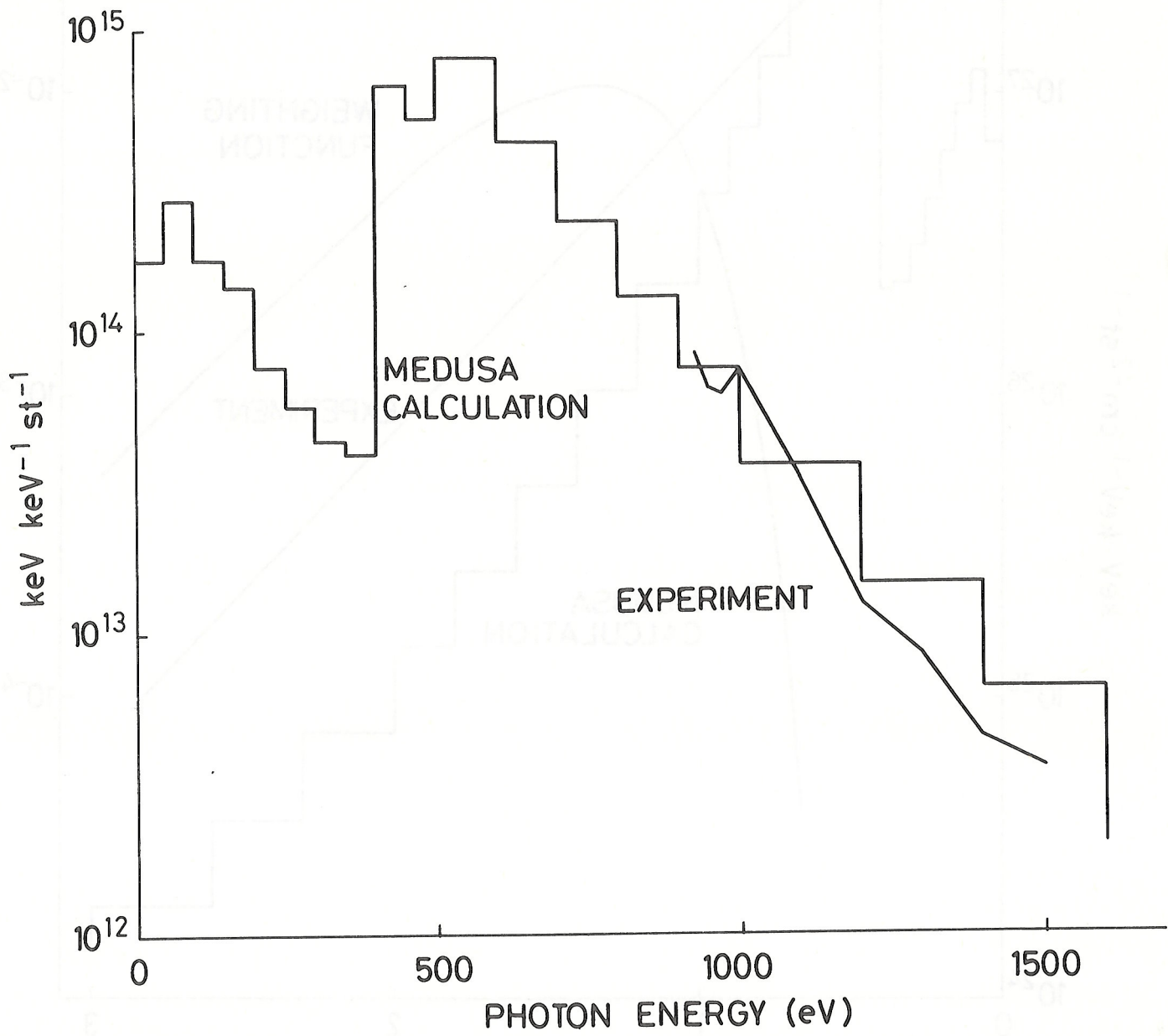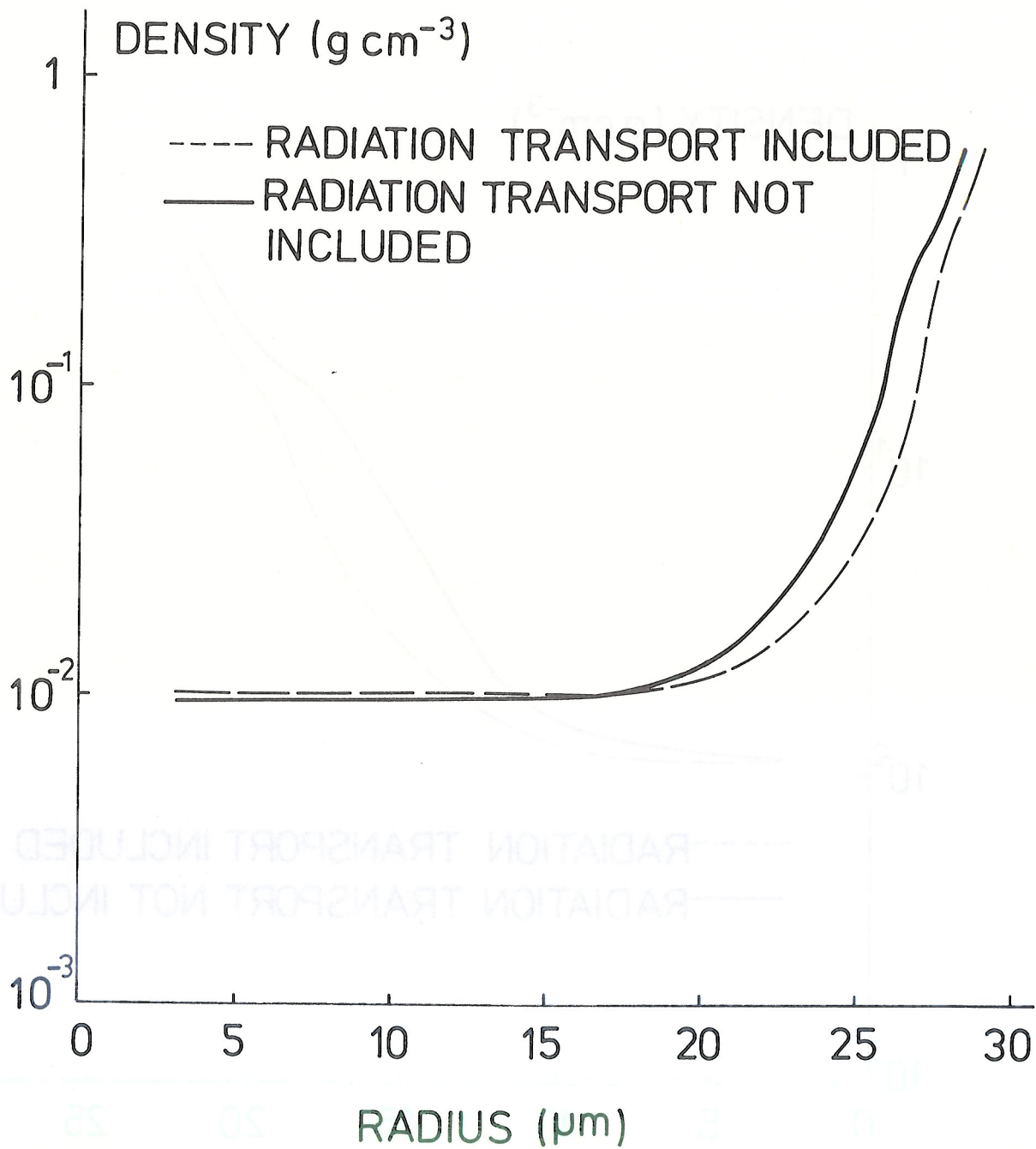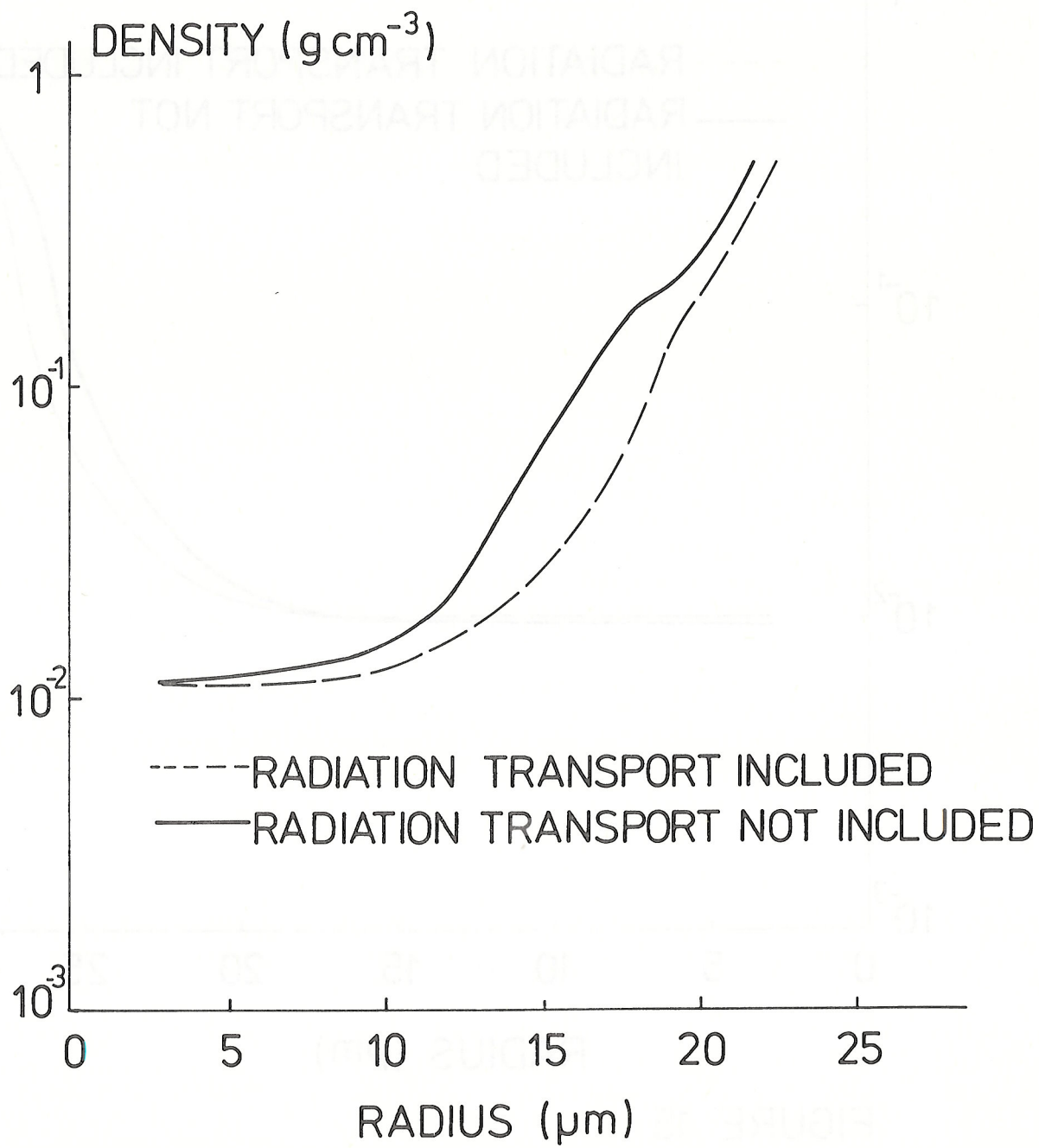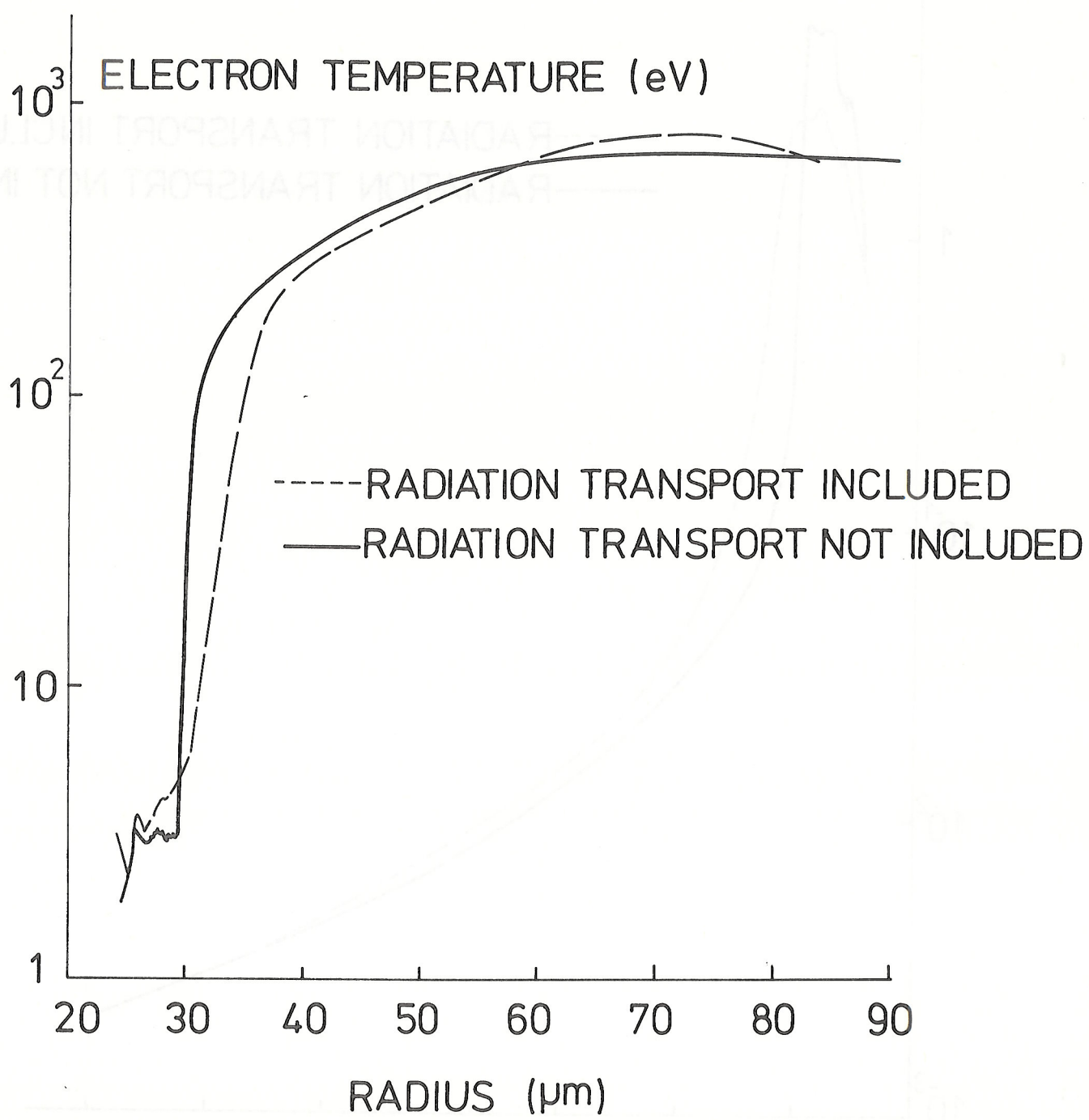
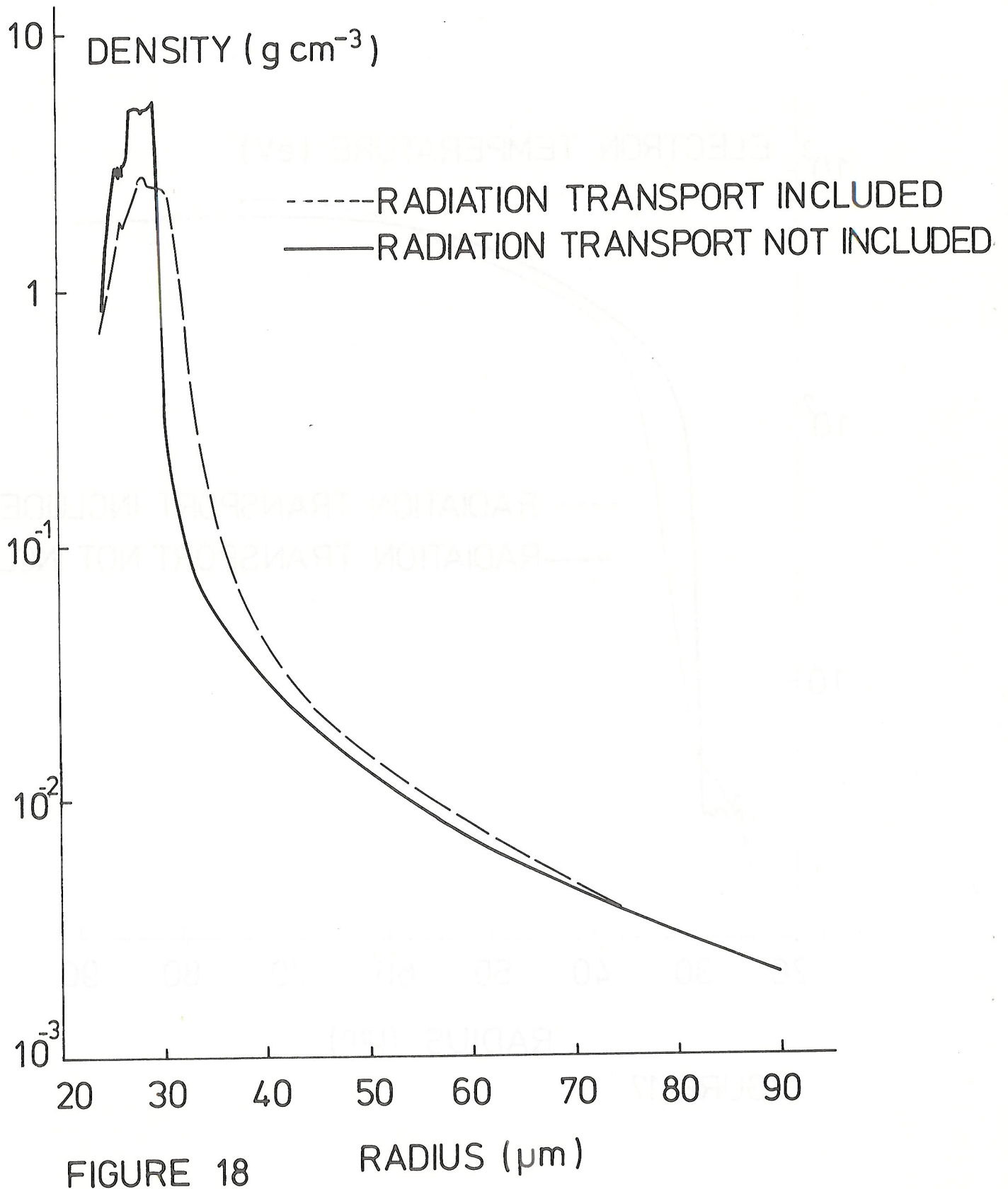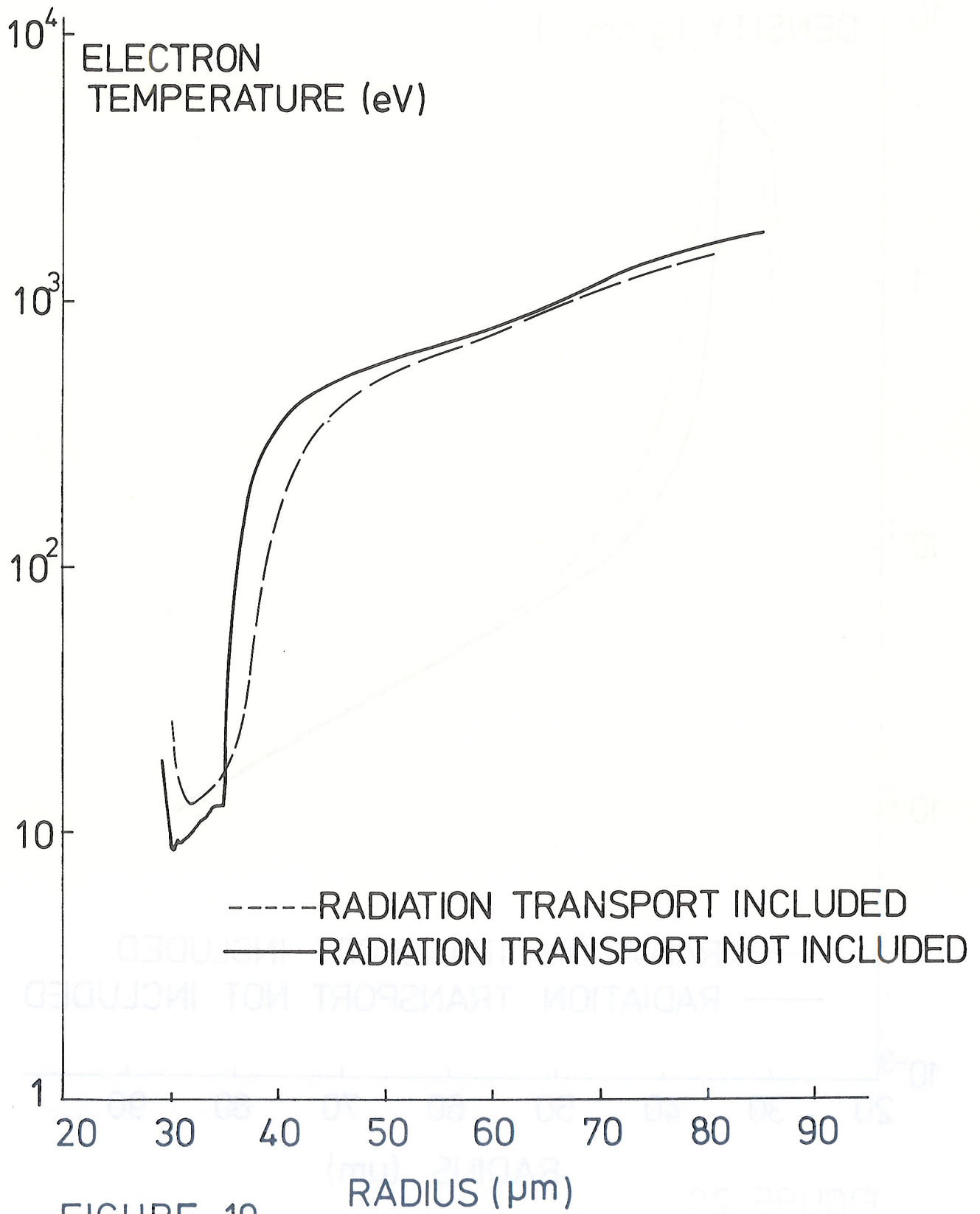FIGURE 1

FIGURE 2
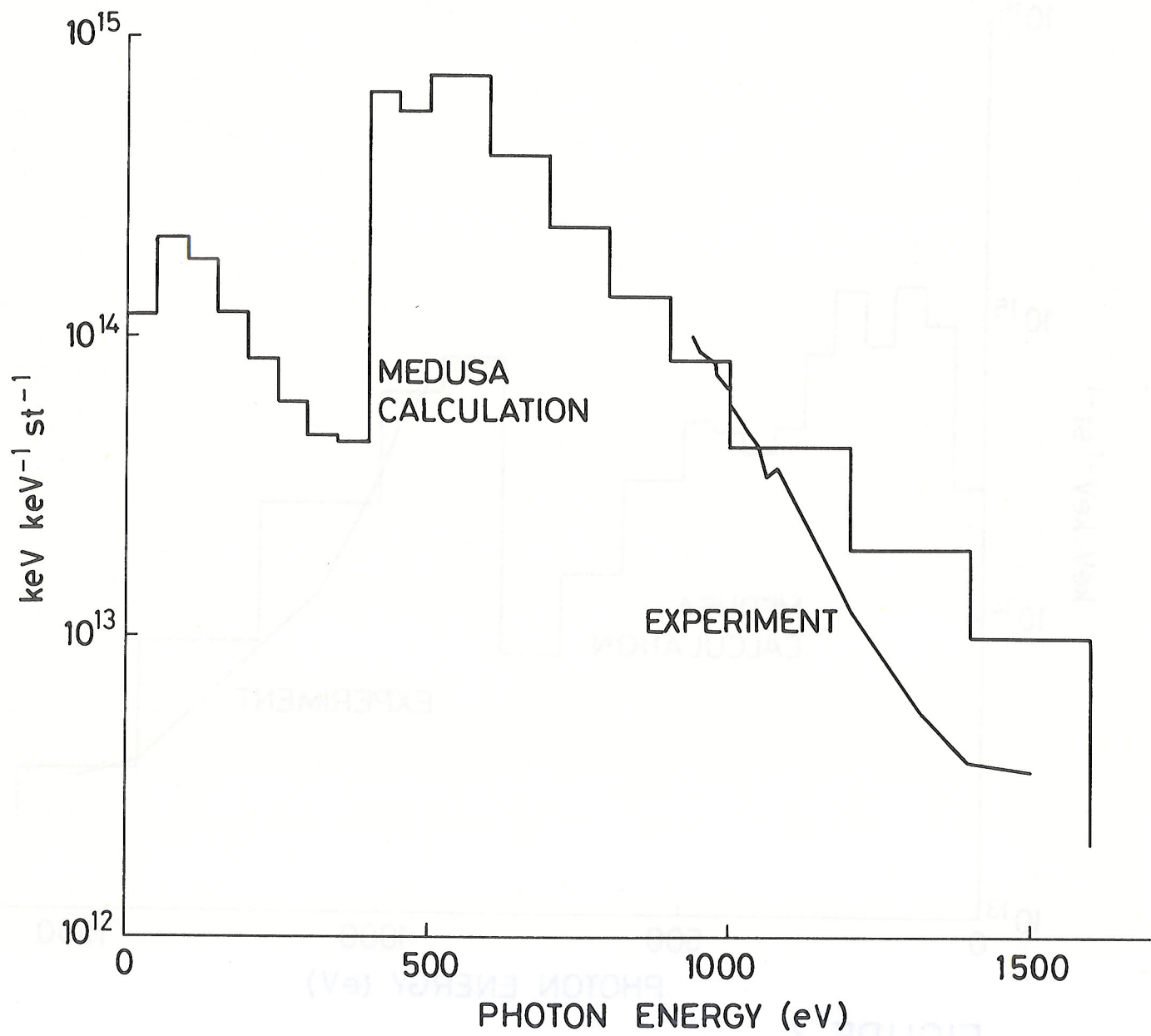
FIGURE 3
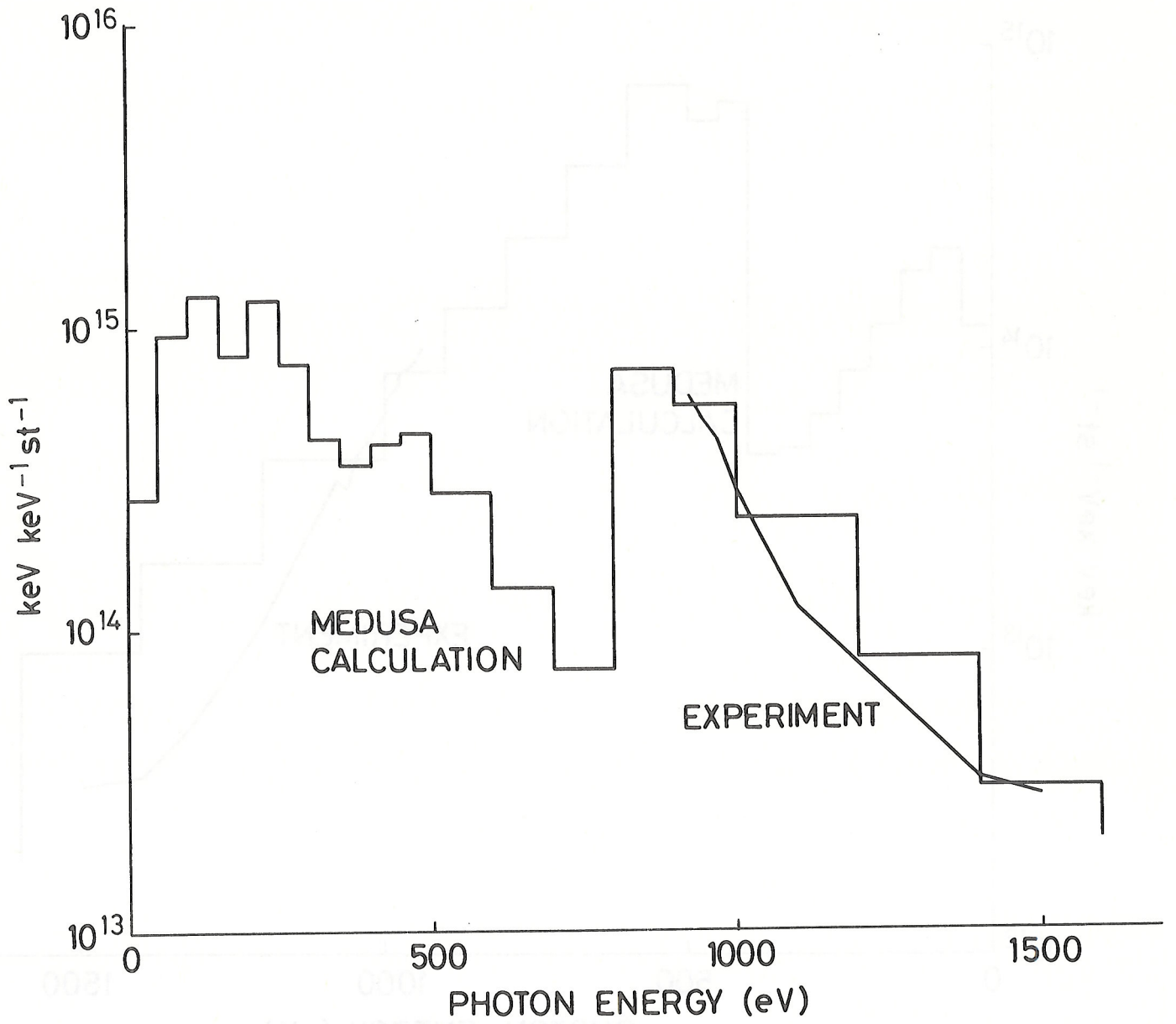
FIGURE 4
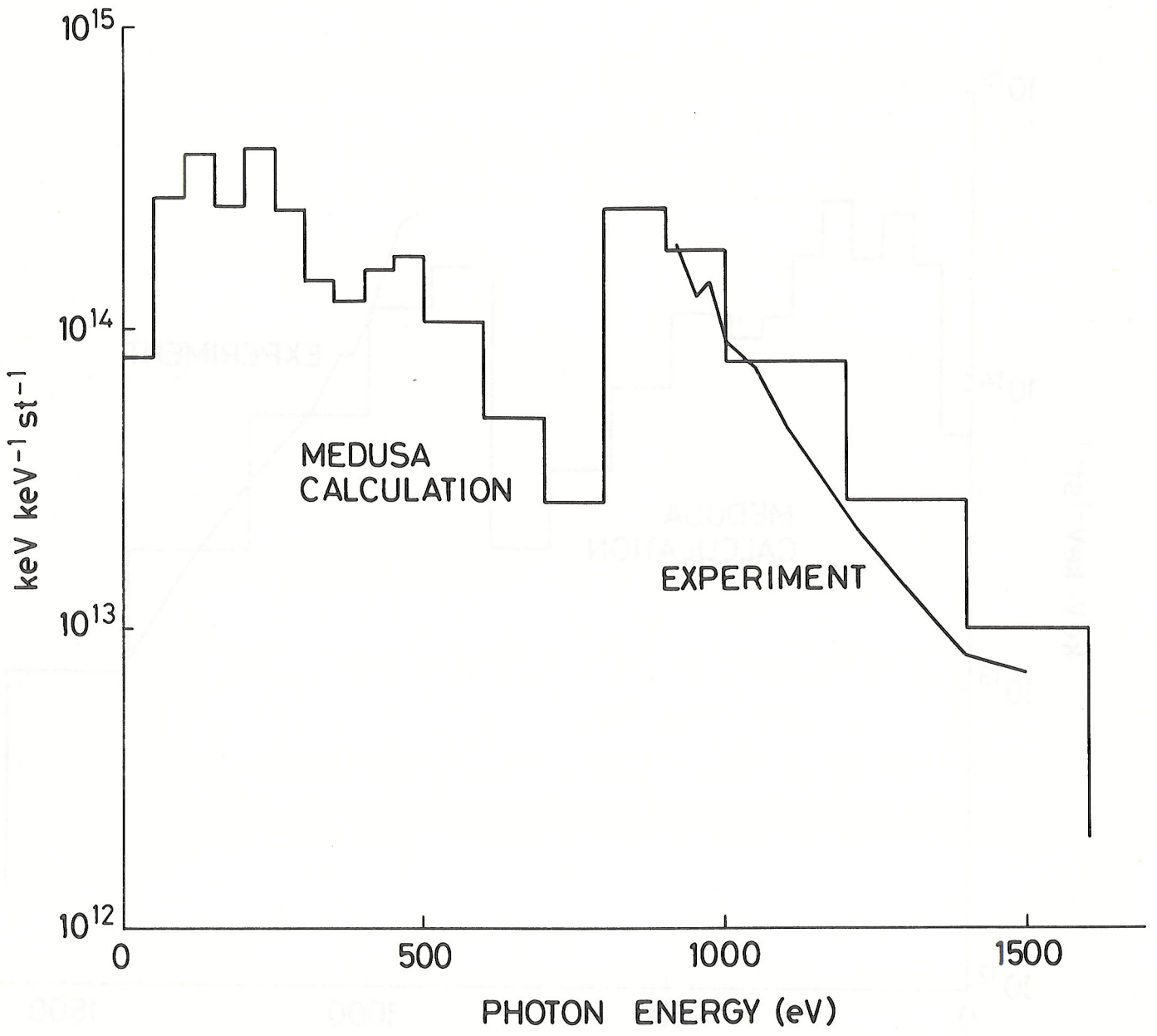
FIGURE 5
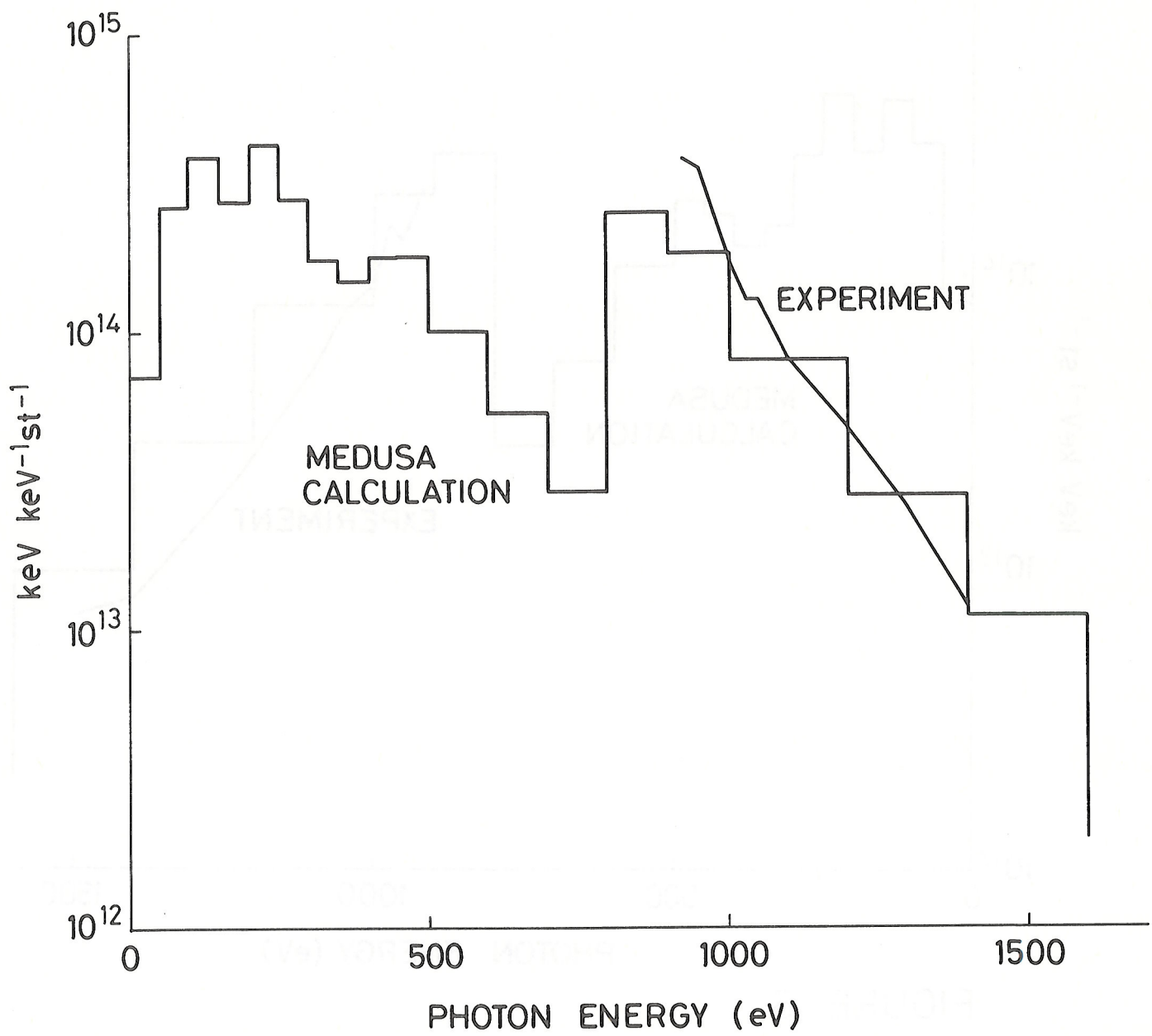
FIGURE 6
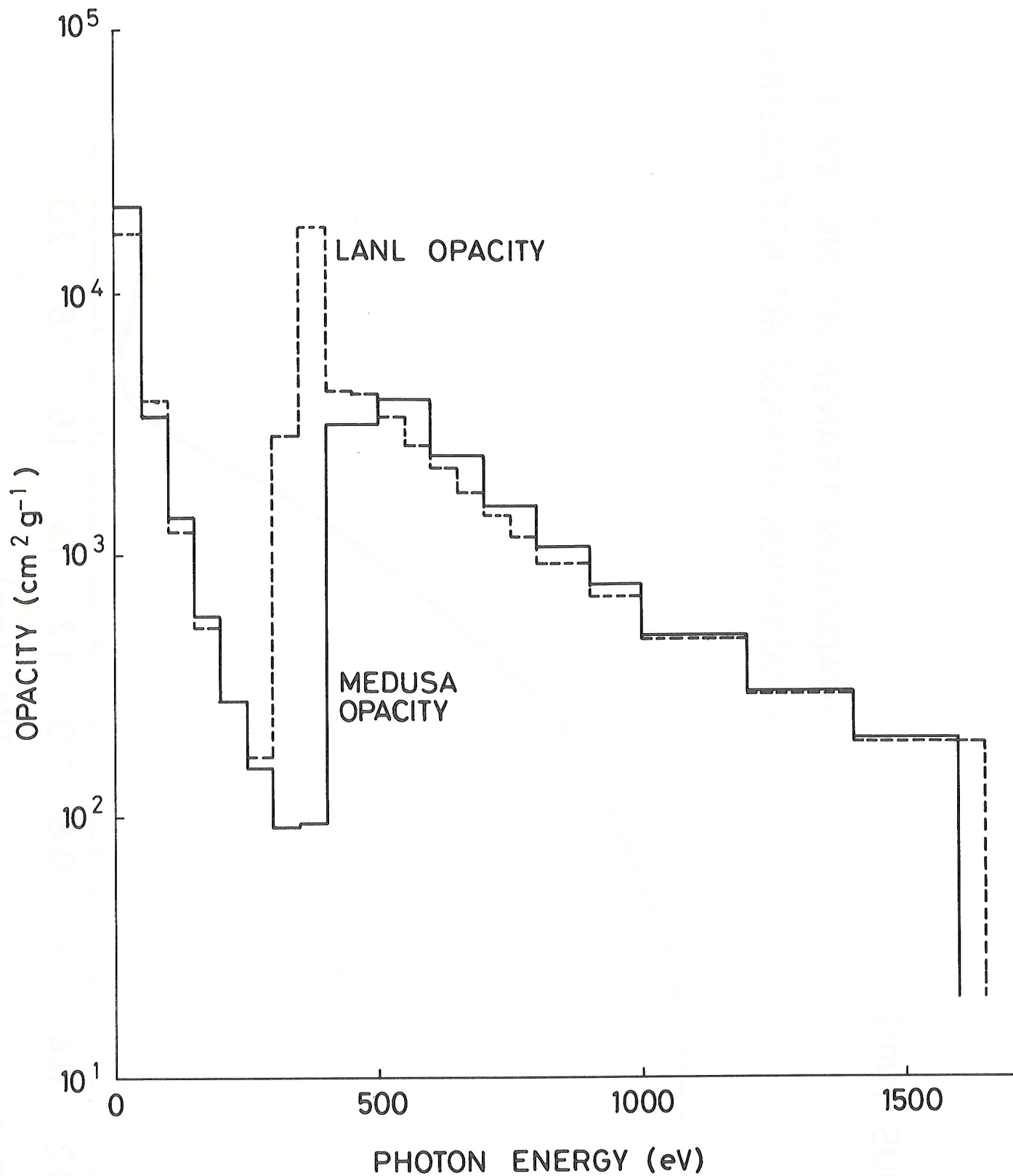
FIGURE 7
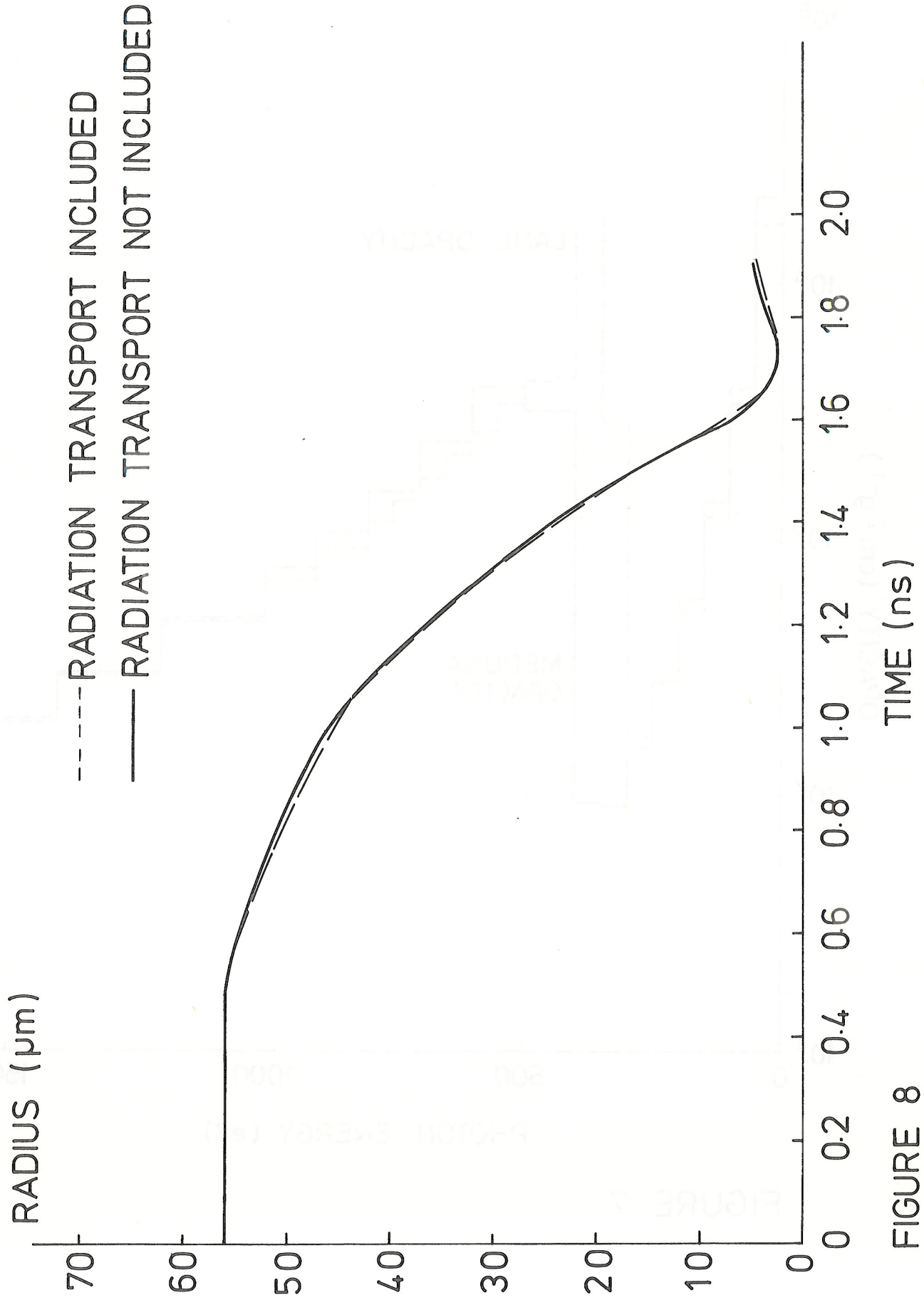
RADIUS (μm)

---- RADIATION TRANSPORT INCLUDED

—— RADIATION TRANSPORT NOT INCLUDED

TIME (ns)

FIGURE 8

RADIUS (μm)

----- RADIATION TRANSPORT INCLUDED

——— RADIATION TRANSPORT NOT INCLUDED

TIME (ns)

FIGURE 9

RADIUS (µm)

----- RADIATION TRANSPORT INCLUDED

——— RADIATION TRANSPORT NOT INCLUDED

TIME (ns)

FIGURE 10

FIGURE 11

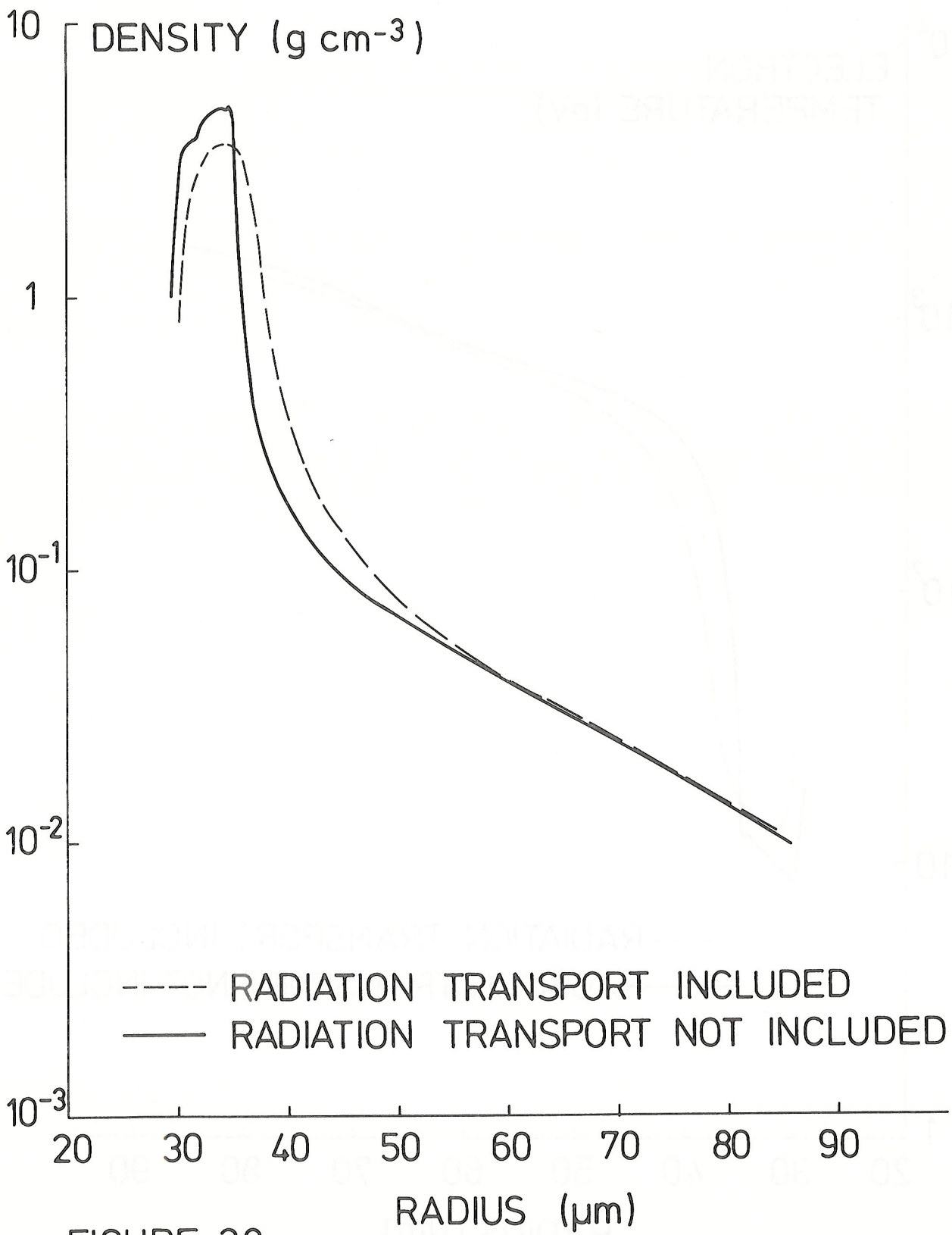TEMPERATURE (eV)

Ti

Te

- - - - RADIATION TRANSPORT INCLUDED
———— RADIATION TRANSPORT NOT INCLUDED

TIME (ns)
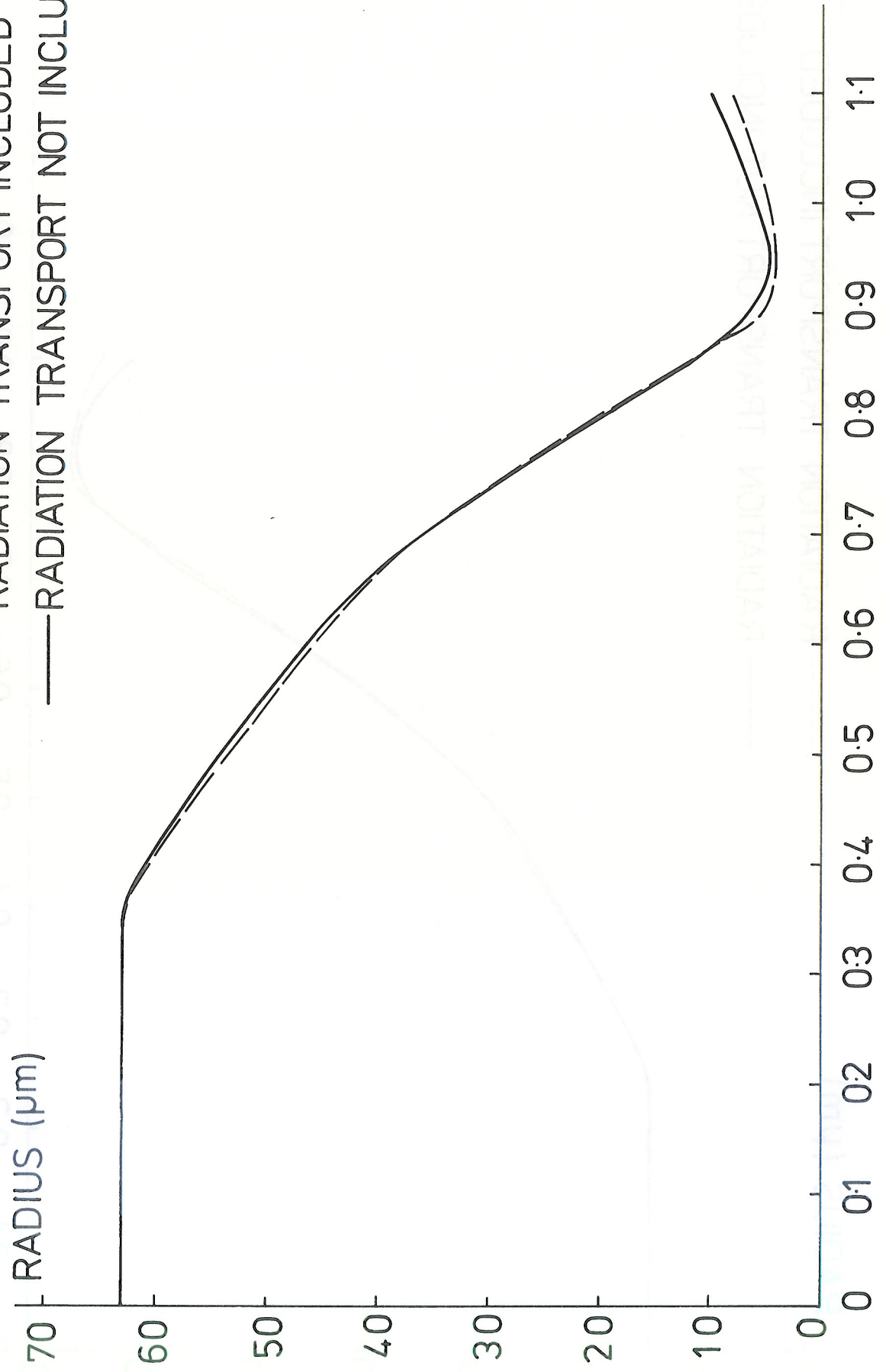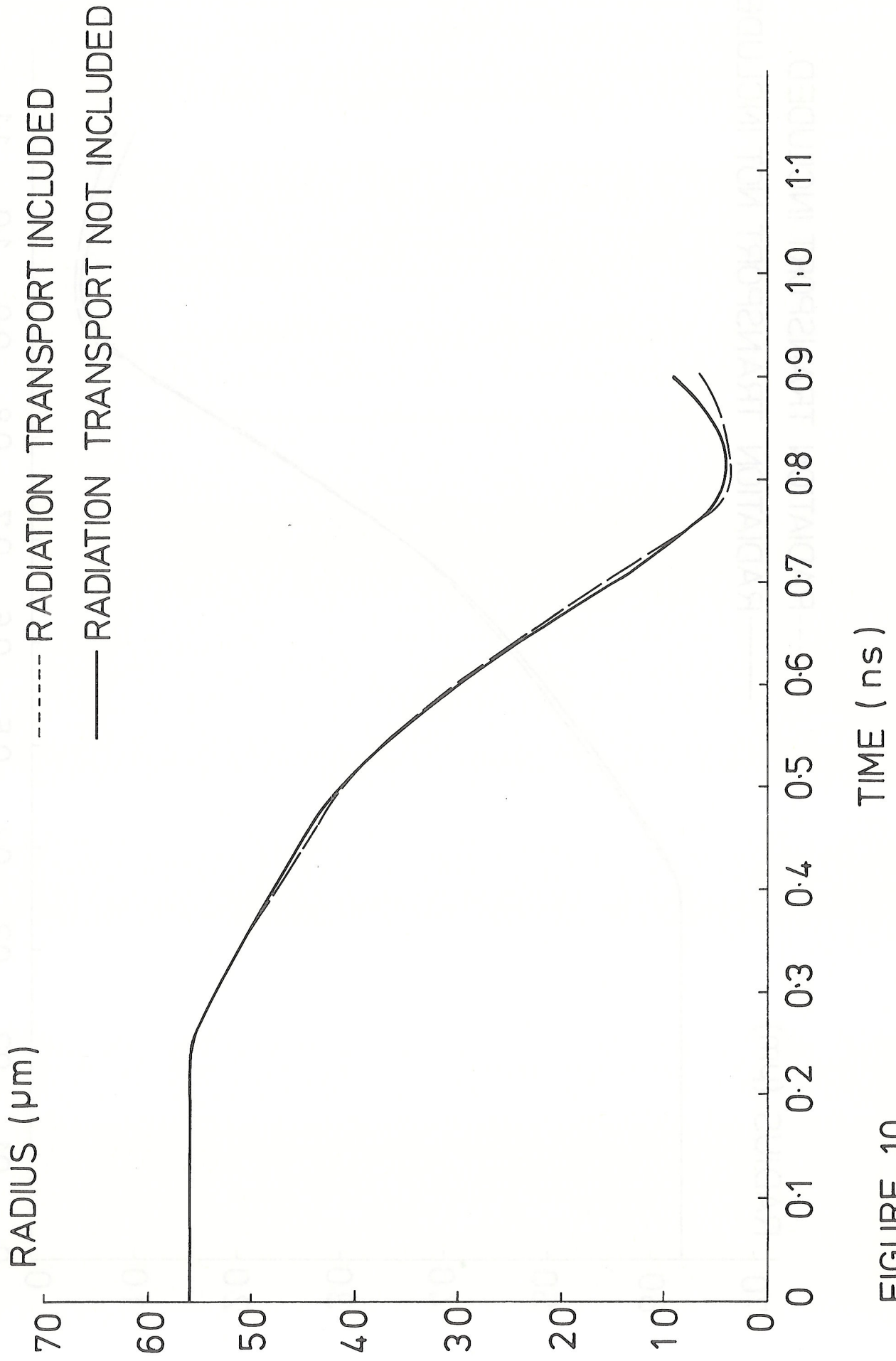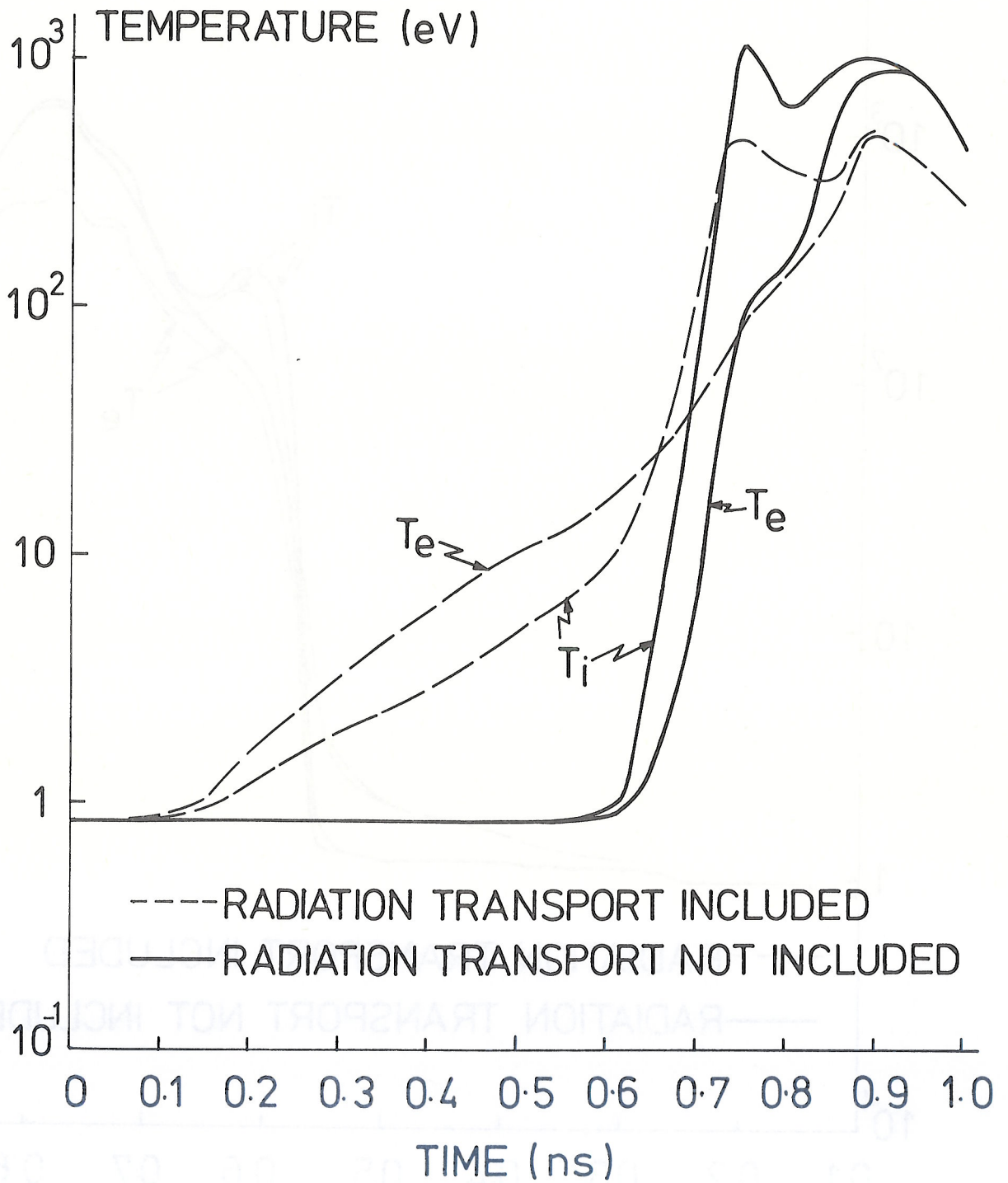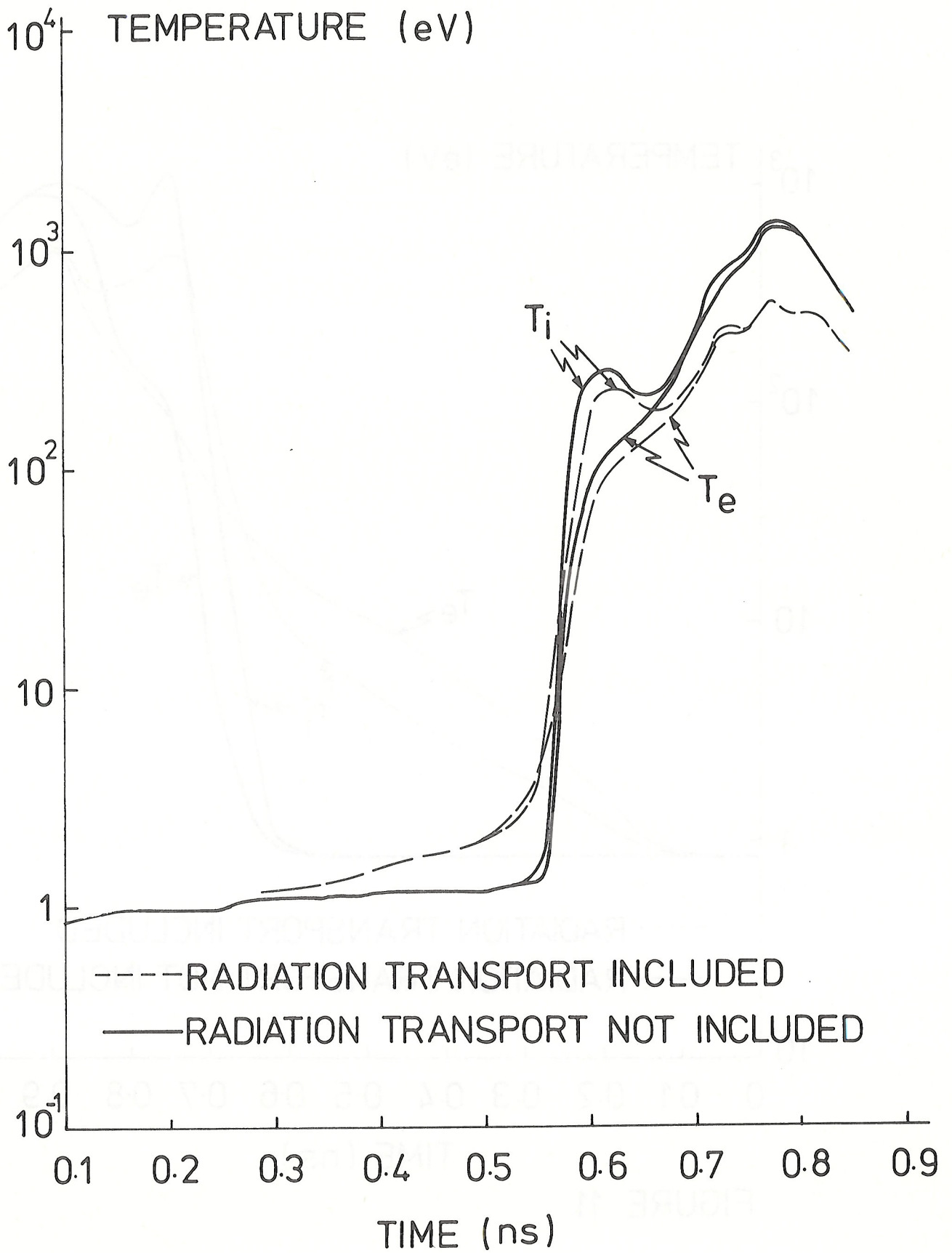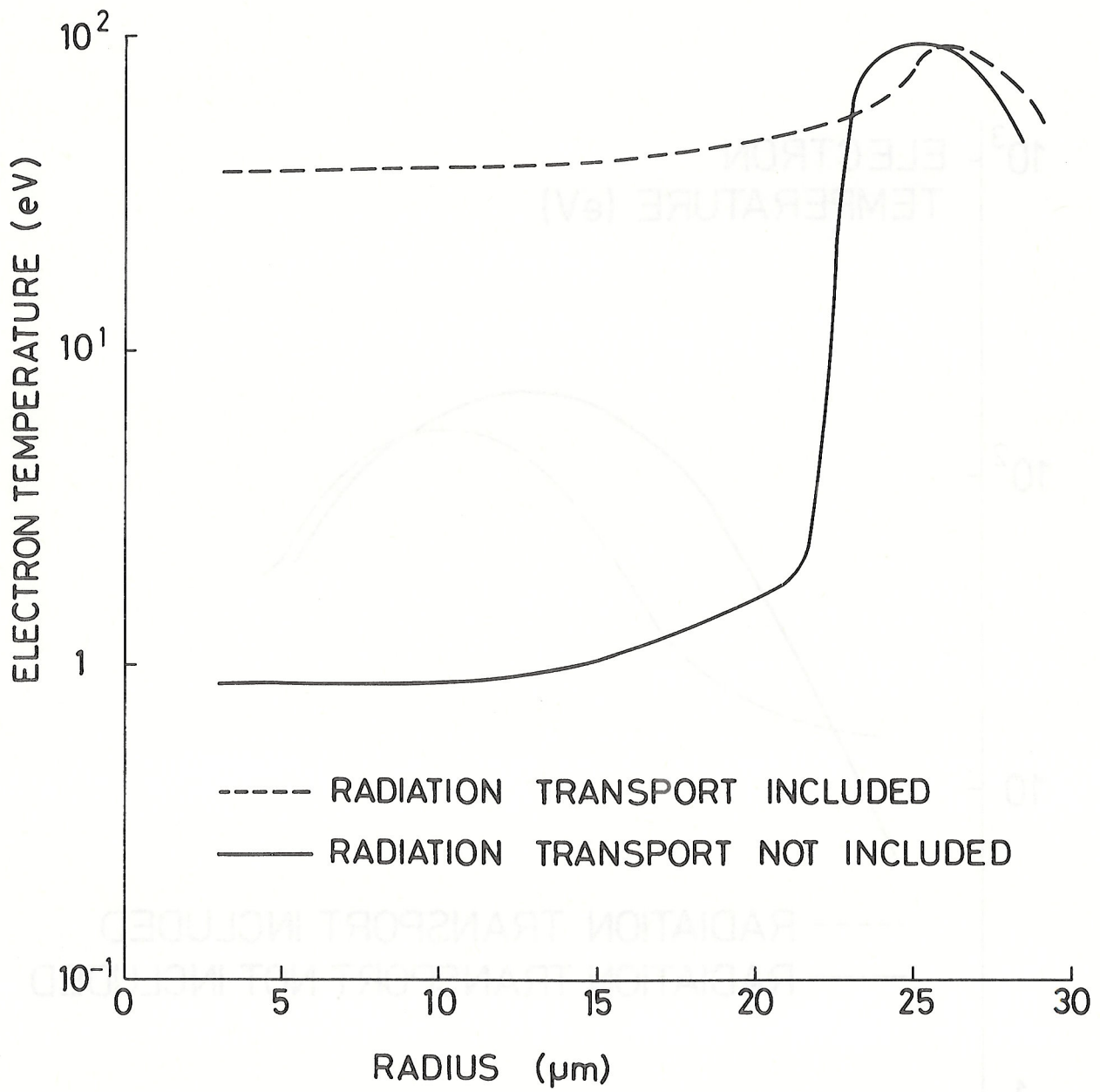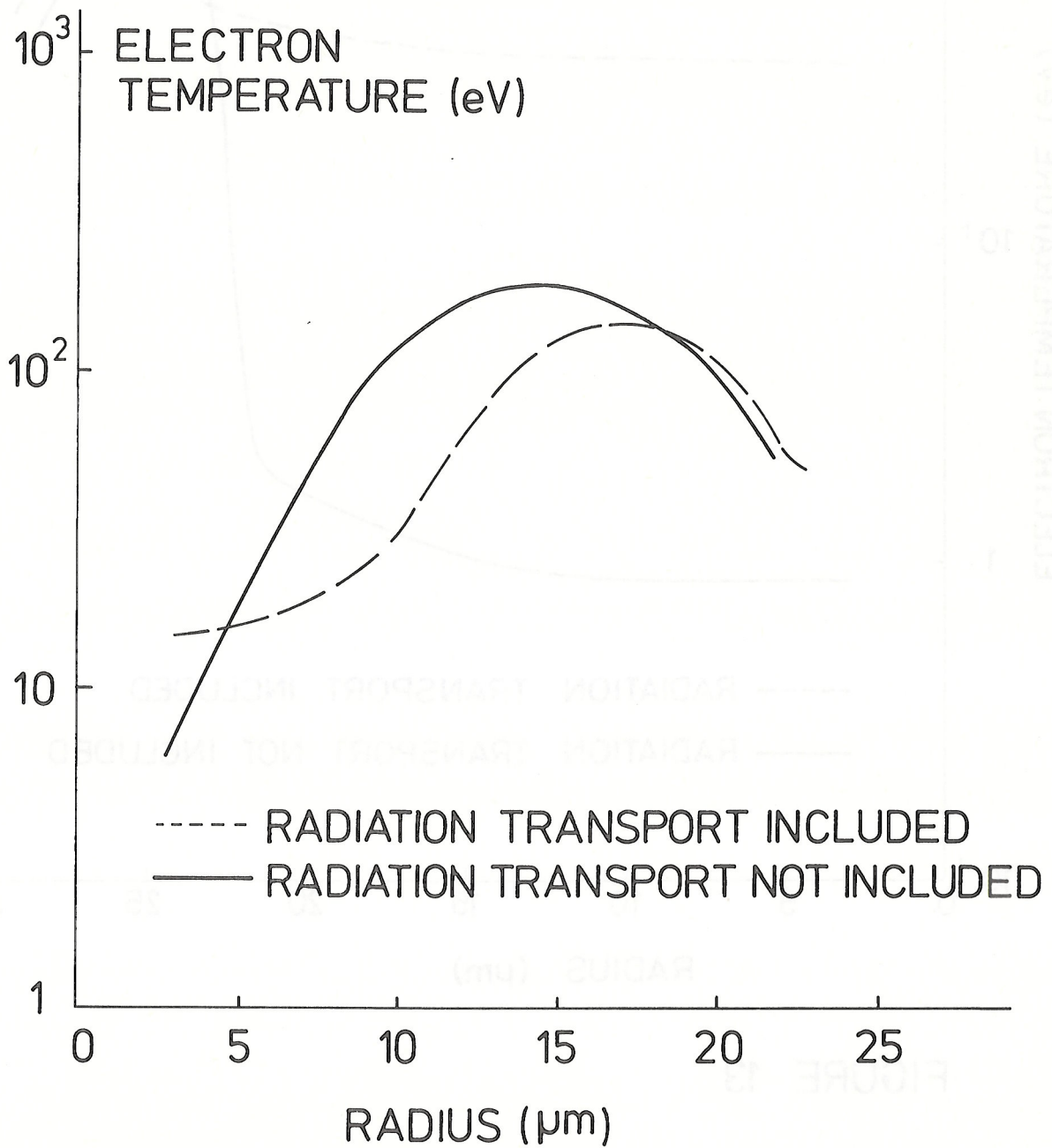
FIGURE 12

FIGURE 13

FIGURE 14

FIGURE 15

FIGURE 16

ELECTRON TEMPERATURE (eV)

-----RADIATION TRANSPORT INCLUDED
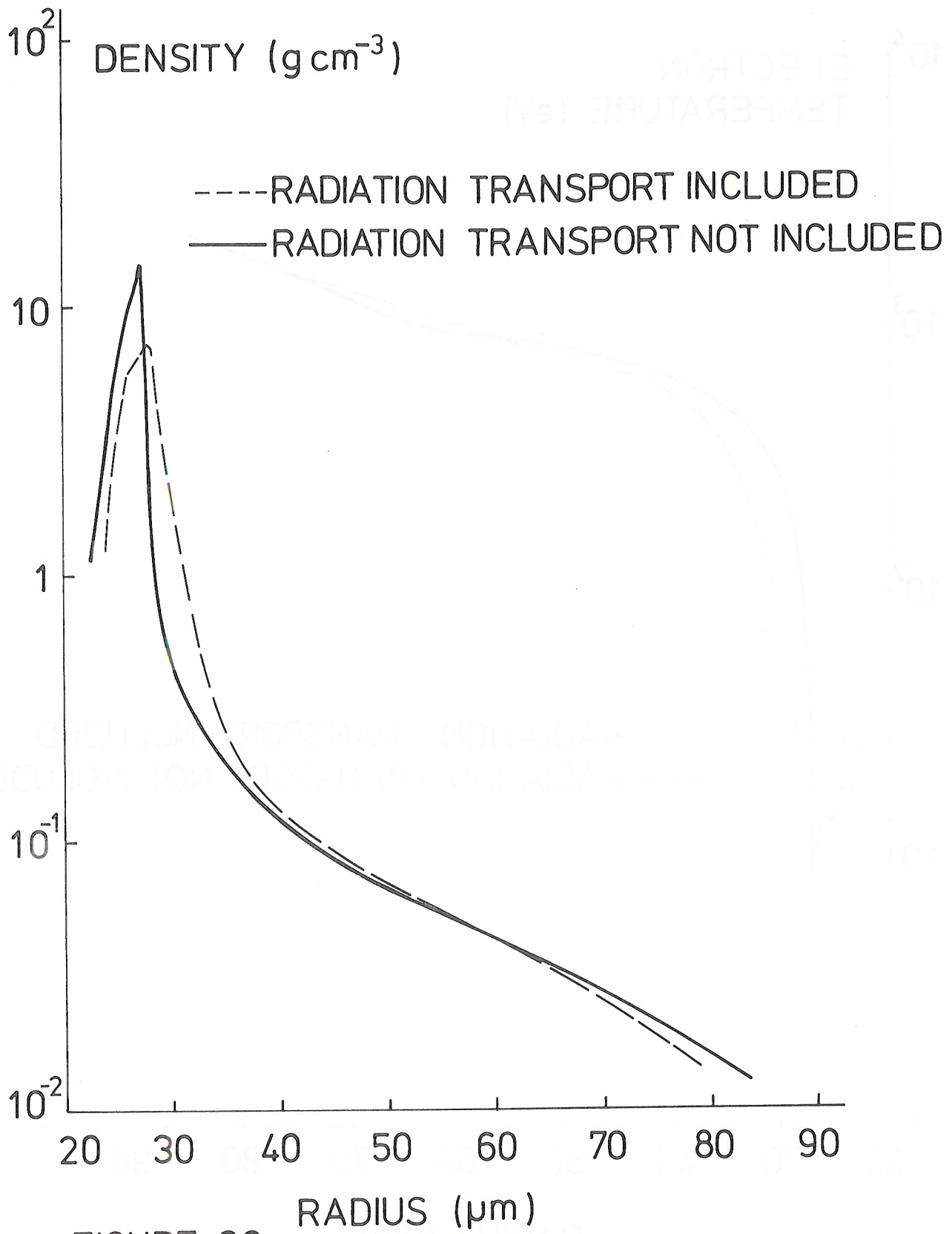———RADIATION TRANSPORT NOT INCLUDED

RADIUS (μm)

FIGURE 17

FIGURE 18

FIGURE 19

FIGURE 20

FIGURE 21

DENSITY ($g\,cm^{-3}$)

−−−−RADIATION TRANSPORT INCLUDED

−−−−RADIATION TRANSPORT NOT INCLUDED

RADIUS (μm)

FIGURE 22